

## TRMM and the global interannual variability of rain over the past five decades

Ziad S. Haddad <sup>1</sup>, Jonathan P. Meagher <sup>1</sup>, Robert F. Adler <sup>2</sup>, Eric A. Smith <sup>2</sup>, Eastwood Im <sup>1</sup>,  
Stephen L. Durden <sup>1</sup>

<sup>1</sup> *Jet Propulsion Laboratory, California Institute of Technology, Pasadena, CA*

<sup>2</sup> *NASA Goddard Space Flight Center, Greenbelt, MD*

**Abstract:** Until 1979, the evidence linking El Niño with changes in rainfall around the world came from rain gauges measuring precipitation over land and a handful of islands. Before the launch of the Tropical Rainfall Measuring Mission (TRMM) in November 1997, the remote sensing evidence gathered since 1979 was confined to ocean rainfall because of the very poor sensitivity of the instruments over land. In this paper we analyze the first five years of the first global land and ocean remote-sensing record of rainfall. We distill the information into a few objective indices, the first principal components of the rain anomaly, and extend them back in time to show how the global remote-sensing record implies that El Niño is indeed the major driver of the global interannual variability of rainfall.

The El Niño / Southern Oscillation (ENSO) phenomenon has been characterized using a few indices calculated from those observables which are most directly related to the physical mechanisms that govern it, namely

- the “El Niño” indices representing an average of the sea surface temperature anomaly within a specified region of the equatorial Pacific Ocean, such as the rather popular “Nino-3” index (see e.g. Trenberth and Stepaniak, 2001),
- the “Southern Oscillation” indices representing the normalized anomaly in the difference between the atmospheric pressure over the Eastern Pacific and that over the Western Pacific / Indian Ocean, and almost always calculated using the measured sea-level pressures (SLP’s) at Tahiti and at Darwin, as in the case of the “Troup SOI” (Troup, 1965),
- the indices directly representing the anomaly in the Walker Circulation (Bjerknes, 1969), such as the 850-mb trade wind index (representing the behavior of the near-surface wind, and calculated from the “reanalysis” of the atmospheric fields estimated from large-scale data-assimilating models – see Latif et al., 1998) or the 200-mb zonal wind at the equator (representing the upper-tropospheric wind, and whose anomalies in the tropics have a most direct effect on the global circulation – see Arkin, 1982).

Thus, the most pertinent observables are the sea surface temperature, the sea-level pressure, and the boundary-layer or upper-tropospheric winds, all of them observed in the tropical Pacific. Also useful are the depth of the thermocline in the Eastern Pacific, and the outgoing longwave radiation

over the tropical Pacific (as a gauge of the frequency and depth of the convective systems).

Yet the observable which has the most immediate impact on people around the globe is neither the strength of the trade winds nor the sea surface temperature nor the atmospheric pressure. Rather, it is the effect of ENSO on the regional change in local rainfall patterns. Numerous studies have documented the link between ENSO and rainfall in many regions of the globe, associating the warm phase with drought conditions in some cases, unusually abundant precipitation in others. The most extensive and detailed study of this kind is undoubtedly Ropelewski and Halpert's (1987, 1988), in which the change in the rainfall sampled over land and island stations within several regions around the globe is carefully analyzed depending on the prevailing ENSO conditions. Indeed, consistent correlations are found between the rain anomaly and the ENSO phase in most of the regions considered (Ropelewski and Halpert, 1987). One could contemplate synthesizing these observations into a global ENSO precipitation index, which would be calculated by adding the rainfall anomalies in all areas which experience excess rain during warm ENSO phases and subtracting the anomaly in those areas which experience a deficit. The problem with such a proposition is that regions which experience excess rain during warm phases do not always experience rain deficits during cold phases and vice versa, as Ropelewski and Halpert (1988) observed. In other words, the maps of the rainfall anomalies during warm or cold ENSO phases do not appear to be mirror images of one another. An equally serious problem with the proposition of subtracting deficit areas from excess areas is that, by subjectively selecting only those areas which have a consistently sustained correlation with ENSO, one would be ignoring those regions which are less significantly affected by the phenomenon, and which could be responsible for a large proportion of the global rainfall variability. This problem was addressed by the objective study of Dai et al (1997), in which a global set of yearly rainfall compiled from land/island station data from 1900 to 1988, was analyzed. After subtracting from the values for each station their mean from 1900 to 1988, and normalizing by the corresponding standard deviation to prevent regions with a large overall variation from overwhelming the subtle change in regions with low rainfall, a principal component analysis of the resulting normalized anomaly was performed. Dai et al found that the first principal component of the normalized annual rain anomaly over the period 1900-1988 was very well-correlated indeed with the bi-monthly average sea-surface temperature anomaly over the equatorial Pacific. While these results are based exclusively on land/island station data which leave vast expanses of ocean unrepresented, they are compelling indicators that ENSO is a very important factor in the variability of rainfall. Thus the accumulated evidence begs the question: how can one objectively quantify the importance of ENSO in the global (land and ocean) variability of surface rainfall?

Until the work of Arkin (1979), Xie and Arkin (1997) and that of Adler et al. (1993) and Huffman et al. (1997), this question had remained unaddressed largely because the systems required to monitor precipitation over the oceans simply did not exist. This dire situation changed dramatically in the 1980's with the availability of data from low-earth-orbiting multiple-frequency microwave radiometers such as the Special Sensor Microwave Imagers (SSM/I), and from geostationary visible/infrared (Vis/IR) imagers. The latter are useful in the sense that they can gauge the height of the cloud tops (and hence, at least in convective systems, the depth of the clouds, and hence, allowing for a quite large uncertainty in one's estimates, the amount of rain which these clouds are producing – see Arkin, 1979), with frequent updates. With less frequent updates, the low-earth-orbit microwave radiometers provide a handful of radiances in which the surface emissivity effects and the competition between the absorption/emission and the scattering from rain and ice can be approximately sorted out to produce an estimate of the rainfall amount at rather poor resolution. Acknowledging the limitations of SSM/I and geostationary IR imagers, Adler et al. (1993) sought to combine them in order to take advantage of the strengths of each and build a “merged” IR-SSM/I/surface-gauge dataset of truly global rainfall, the Global Precipitation Climatology Project (GPCP; see Huffman et al., 1997). An “ENSO precipitation index” (ESPI) is currently calculated from GPCP, essentially by subtracting the precipitation anomaly over the region around the Maritime Continent ( $10^{\circ}\text{S} - 10^{\circ}\text{N} \times 90^{\circ}\text{E} - 150^{\circ}\text{W}$ ) from that over the eastern Pacific ( $10^{\circ}\text{S} - 10^{\circ}\text{N} \times 160^{\circ}\text{E} - 100^{\circ}\text{W}$ ) – the exact boundaries of the boxes are “dynamically” calculated in real-time to maximize the contrast. By design, ESPI correlates very well with the “El Niño” and “Southern Oscillation” indices (Curtis and Adler, 2000). Going one step further, Xie and Arkin (1997) folded in numerical model predictions as well, and produced the “CMAP” global dataset of monthly surface rainfall estimates from 1979 to 1995 on a  $2.5^{\circ}$  grid. Their maps of the seasonal difference (warm phase - cold phase) of the rainfall anomaly averaged over the 17 years of data incorporated in CMAP confirmed many of the results of Ropelewski and Halpert, and Dai and Wigley's principal component analysis of the normalized annual rain anomaly (Dai and Wigley, 2000) yielded a 20-point time series (CMAP had by then been updated to 1998) which matches the SOI over that period remarkably well. These first truly global results depend ultimately on the reliability of the sources of the data, namely the IR and SSM/I estimates. As we have already noted, the former relies on the statistically-derived correlation between cloud top heights and surface rain, which has a large intrinsic uncertainty and whose applicability depends on precipitation type. While SSM/I is more directly sensitive to the rain itself, the poor resolution of the instrument forces one to make homogeneity assumptions about the precipitation which are likely to introduce large biases in the estimates (because the average rain quantities one would like to estimate are related in a very non-linear way to the average radiances one measures). Most important, over land, the relation between

either the IR or the microwave radiances and the surface precipitation is tenuous at best.

It is precisely to remedy the shortcomings of these systems (their poor resolution and their lack of much direct sensitivity to the vertical structure of precipitation) that the Tropical Rainfall Measuring Mission (TRMM) was conceived and the TRMM satellite launched in November, 1997 (Simpson et al., 1988). In addition to having a very low resolution-enhancing orbit (originally 350 km), TRMM's advantage is that it carries the first spaceborne precipitation-profiling radar (PR), in addition to a nine-channel microwave radiometer (TMI) and a visible/infrared imager. Although the clutter from the overwhelming surface echo severely limits the swath of the PR and, therefore, limits its ability to sample the precipitation as frequently as a radiometer, the vertical detail with which it can probe the atmosphere, its insensitivity to the characteristics of the surface, and its high horizontal resolution ( $\simeq 4$  km) make it an ideal instrument with which to "calibrate" the rain retrievals of the radiometer within the narrow common swath of the radar (Haddad et al., 1997), and subsequently carry this calibration over to the TMI-only retrievals over the wide swath of the radiometer (Adler et al., 2000).

Of particular interest are the surface rainfall estimates produced by this "TRMM-combined" radar/radiometer algorithm from December 1997 until the present. These estimates are available in the form of monthly rain maps over the region between  $40^{\circ}\text{S}$  and  $40^{\circ}\text{N}$  at a resolution of  $5^{\circ} \times 5^{\circ}$ . To synthesize the information in these maps objectively, we performed principal component analyses of the rainfall estimates and of their anomalies. Figure 1 illustrates the results. It displays the coefficients

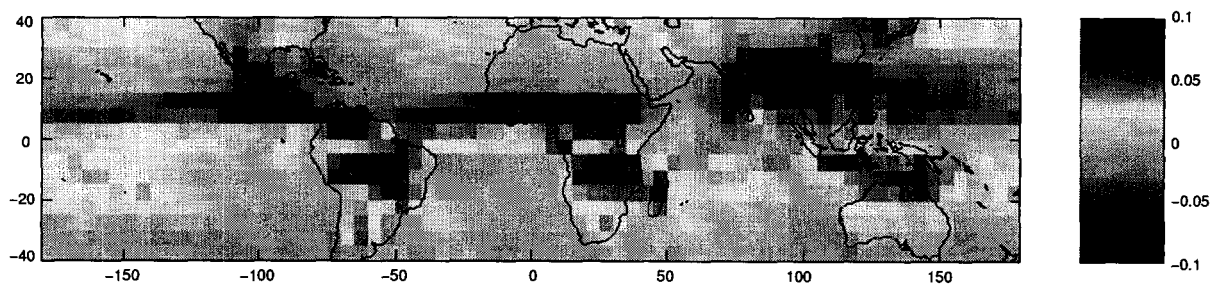


Fig. 1. Coefficients of the first principal component of the TRMM-combined monthly rainfall averages, for the 60 months of data from 1/98 to 12/02 (Note that there are  $(80 \times 360)/(5 \times 5) = 1152$  pixels, so the reference value for the coefficients is  $1/\sqrt{1152} \simeq 0.03$ ).

of the first principal component of the TRMM-combined monthly rainfall accumulation. As expected, the linear combination of pixels which captures the greatest share of the monthly variability (about 33%) in the rainfall is obtained essentially by subtracting the pixels with a November-to-

April rain peak from the ones with a May-to-October rain peak, reflecting the simple fact that the seasons are indeed the major driver of the change in rainfall patterns from month to month. Much more interesting is the characterization of the variation of the monthly rain anomaly. Using the 60 months' worth of TRMM-combined data from January 1998 to December 2002 as the baseline to establish the monthly mean for each pixel, we performed a principal component analysis on the monthly TRMM-combined rain anomaly. The coefficients of the first three principal components

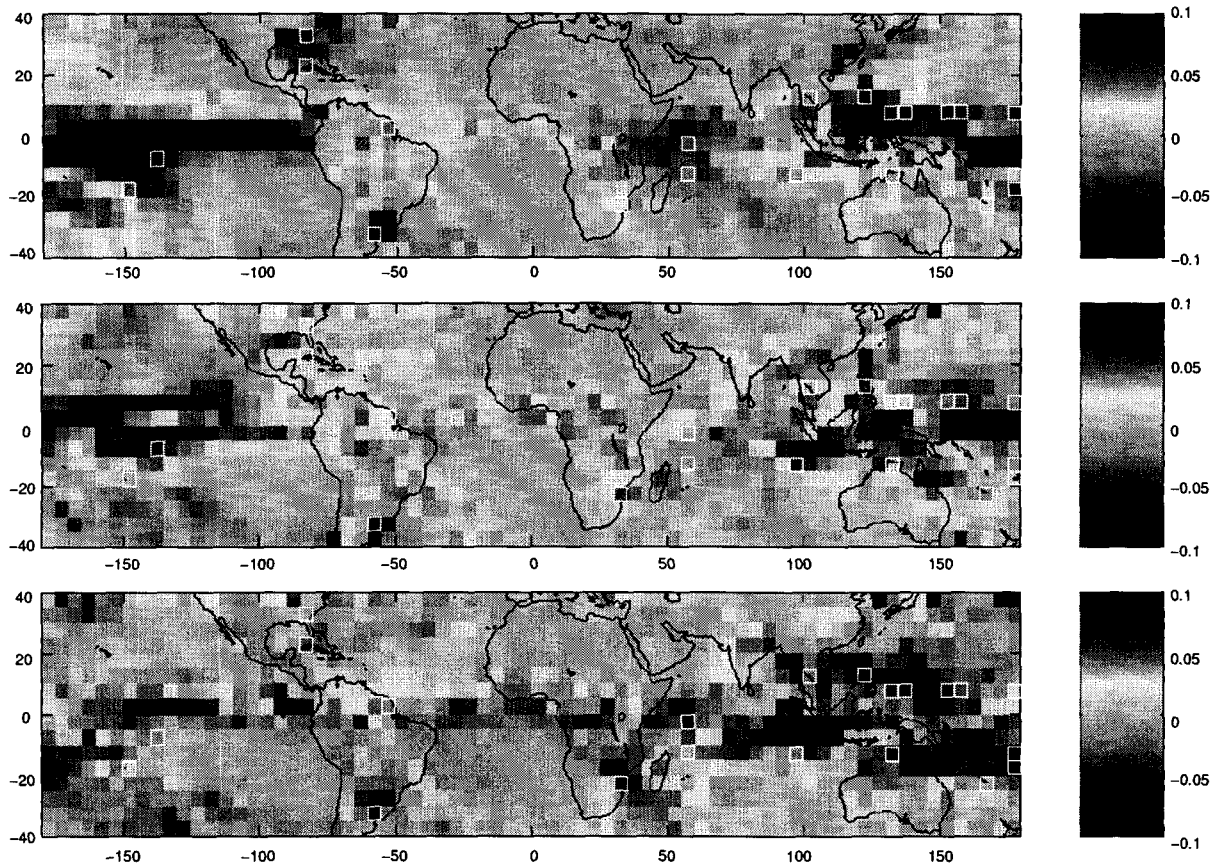


Fig. 2. Coefficients of the first three principal components  $PC_1$  (top panel),  $PC_2$  (middle panel) and  $PC_3$  (bottom panel) of the TRMM-combined monthly rainfall anomalies, for the 60 months of data from 1/98 to 12/02 (the reference value for the coefficients is approximately 0.03).

$PC_1$ ,  $PC_2$  and  $PC_3$  (ranked according to their variance in decreasing order) are shown in figure 2.  $PC_1$  accounts for about 14% of the variability,  $PC_2$  accounts for another 7%, and  $PC_3$  for a further 5%. As to the coefficients themselves, one readily notes that the variability of the rainfall anomaly is strongly sensitive to the precipitation over the oceans, in rather sharp contrast with the variability of the rainfall itself which, as figure 1 shows, is more sensitive to continental rainfall. This is due to the more rapid and pronounced response of the continents to summer heating (resp. winter cooling), which enhances (resp. inhibits) the rain-producing convection. In contrast, the tropical

Western Pacific and the equatorial Eastern Pacific have large coefficients in all three principal components of the rain anomaly. This is undoubtedly due in no small part to the fact that the TRMM record starts in the middle of one of the strongest ENSO warm phases of the twentieth century. However, the signs of the coefficients of the principal components over the various pixels within the Pacific do not seem clearly consistent enough to make an objective link between the rainfall anomaly and ENSO.

In order to understand in more detail and eventually quantify how the principal components of the rain anomaly do correlate with the physical mechanisms which directly affect rainfall, it is important to find a way to extend the TRMM observations in general, and the anomaly index  $PC_1$  in particular, beyond the five years' worth of TRMM data. We attempted to achieve this by making use of the Global Historical Climatology Network (GHCN) rainfall dataset (Peterson and Vose, 1997), which provides monthly surface rain accumulations from over 20,000 surface stations. We started by distinguishing those TRMM pixels whose coefficients in the first three anomaly principal components are large in absolute value, and for which there exists at least one surface station in the GHCN database with a reasonably complete observational record extending to December 2002 (i.e. overlapping the TRMM record) and reaching back at least to the 1950's or earlier. We thus identified 21 pixels (highlighted in white in figure 2) and 21 corresponding surface stations, listed in table 1. Note that five of these stations are in Micronesia, whose rain anomaly Ropelewski and

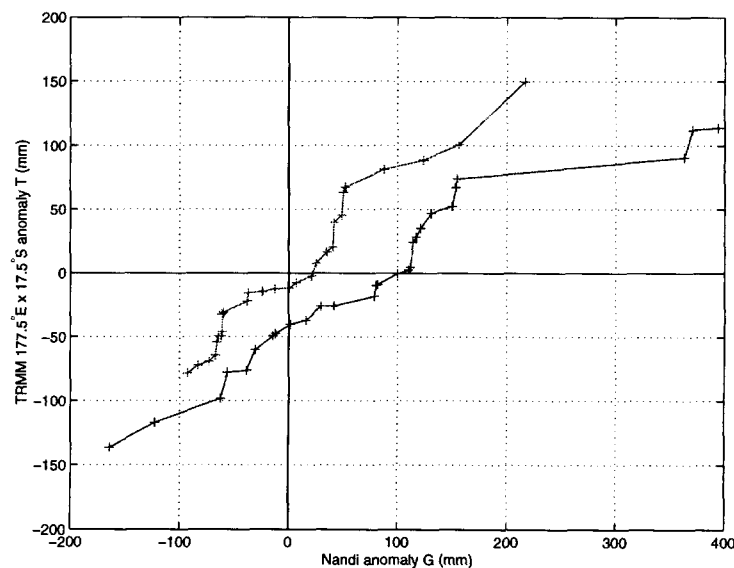


Fig. 3. Relations between the ground-station-anomaly  $G$  and the TRMM-pixel-anomaly  $T$  for Nadi and the pixel centered at  $177.5^\circ\text{E}$   $17.5^\circ\text{S}$  (November-April in blue, May-October in red).

Halpert found not to correlate consistently with ENSO. Next, one must account for the fact that the

Lon	Lat	PC <sub>1</sub> coefficient	GHCN Station	TRMM-pixel $\simeq a + b \cdot$ (GHCN-station)	
				May-to-Oct ( $a, b$ )	Nov-to-Apr ( $a, b$ )
57.5°W	32.5°S	-0.083	Buenos Aires	(1.3, 74)	(0.83, 49)
122.5°E	12.5°N	0.078	Legaspi	(0.8, 59)	(0.56, -80)
152.5°E	7.5°N	0.078	Truk	(0.5, -43)	(0.58, -60)
137.5°E	7.5°N	0.073	Yap	(0.47, -63)	(0.78, -9)
157.5°E	7.5°N	0.071	Pohnpei	(0.54, -86)	(0.42, -85)
177.5°E	17.5°S	0.066	Nadi (Fiji)	(0.74, 0)	(0.48, -45)
132.5°E	7.5°N	0.064	Koror (Palau)	(0.57, -65)	(0.37, -42)
82.5°E	27.5°N	-0.060	Jacksonville	(0.54, -15)	(1.0, 39)
172.5°E	7.5°N	0.049	Majuro	(0.48, -56)	(0.4, -32)
52.5°W	7.5°N	0.042	Cayenne	(0.43, -47)	(0.3, -42)
137.5°W	7.5°S	-0.039	Hiva Oa	(0.47, -33)	(0.37, -31)
97.5°E	12.5°S	0.038	Cocos Is.	(0.57, -25)	(0.55, -38)
102.5°E	12.5°N	0.034	Bangkok	(0.5, 3)	(1.1, 27)
177.5°E	12.5°S	0.032	Rotuma (Fiji)	(0.83, -79)	(0.8, -72)
32.5°E	22.5°S	0.030	Inhambane	(1.0, 0)	(1.0, 0)
167.5°E	22.5°S	0.029	Noumea	(1.13, 7)	(0.52, -4)
57.5°E	12.5°S	-0.027	Agalega Is.	(0.46, -12)	(0.4, -36)
147.5°W	17.5°S	-0.025	Tahiti	(1.1, 25)	(0.45, -16)
82.5°W	22.5°N	-0.025	Key West	(0.62, 11)	(1.0, 16)
57.5°E	2.5°S	-0.023	Mahe	(0.3, -12)	(0.33, -59)
132.5°E	12.5°S	0.013	Darwin	(0.72, 1)	(0.46, -51)

TABLE I

THE 21 PIXELS AND ASSOCIATED STATIONS, AND THEIR CORRESPONDING CONTRIBUTION TO THE CALCULATION OF THE MONTHLY RAINFALL ANOMALY VARIABILITY INDEX.

surface station accumulations are not perfectly representative of the amounts TRMM would have estimated over the corresponding pixel. If one had a large amount of  $5^\circ \times 5^\circ$  anomaly data  $\{T\}$  (normalized relative to the TRMM-combined 1/98-12/02 baseline) carefully classified according to the underlying rain regime, along with the corresponding surface station anomalies  $\{G\}$  (calculated relative to the same baseline), it would not be unreasonable to postulate a direct relation  $T = f(G)$  with  $f$  depending on the particular location and the particular rain regime. Under this hypothesis, the best way to estimate  $f$  from the data is to match the cumulative distributions of  $G$  and  $T$  (Haddad and Rosenfeld, 1997). We performed separate probability matches for the 21 stations for each of two seasons, May-to-October and November-to-April. The resulting probability-matching functions  $f$  are illustrated in figure 3 for the pixel  $177.5^\circ\text{E} \times 17.5^\circ\text{S}$  represented by the ground station at Nadi, Fiji. Linear fits for all 46 probability-matching  $G$ - $T$  relations are shown in table

1. Using them, we can now define a “proxy”  $PC'_1$  for the first TRMM-combined anomaly index  $PC_1$ : indeed, where the latter was a combination  $PC_1 = \sum a_n T_n$  over all 1152 pixels, define the proxy to be the sum  $PC'_1 = c \sum_{n=1}^{21} a_n f_n(G_n)$  over the 21 stations, with the same TRMM-combined coefficients  $a$ , and where  $f_n$  is the probability-matching station-pixel relation for the  $n^{\text{th}}$  pixel and the appropriate season (May-to-October or November-to-April), and where the sum has to be re-normalized by the factor  $c = \sqrt{1152/21}$ . The comparison between the actual TRMM-combined index  $PC_1$  and its 21-station proxy  $PC'_1$  is shown in figure 4. As the figure suggests, we can now compare  $PC'_1$  to any climatological index over the past few decades. The obvious candidates for

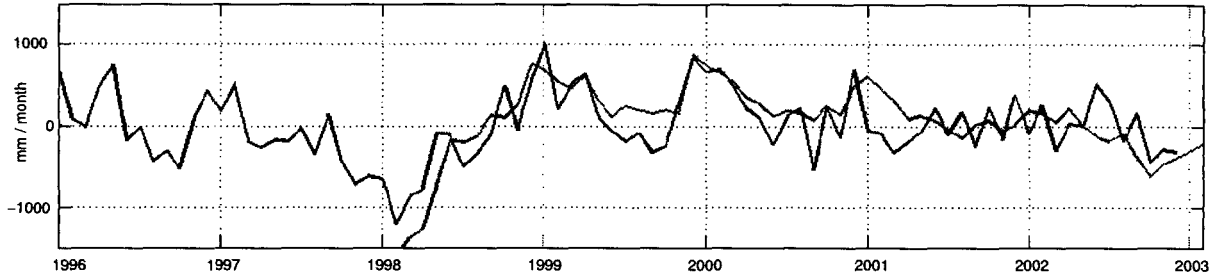


Fig. 4. The time-series of the TRMM-combined anomaly  $PC_1$  (red), and of its 21-station fit  $PC'_1$  (blue).

such a comparison are the ENSO indices, and figure 5 shows the graphs of  $PC'_1$  and the Troup SOI calculated as

$$SOI = 10 \frac{[\text{Tahiti SLP} - \text{Darwin SLP}] - \text{mean}}{\text{standard deviation}}$$

where the mean and standard deviation are calculated over the period from 1887 until 1989. The scaling factor  $\lambda = 0.027$  which was used to change the units of  $PC'_1$  was obtained by minimizing the conditional mean-squared distance between  $\lambda PC'_1$  and SOI, over those months where SOI exceeds 1.5 times its standard deviation (in order to avoid fitting noise). The correlation coefficient was 0.65, and this already respectable value exceeds 0.7 if the correlation is calculated only for those samples where either index exceeds 1.8 times the standard deviation of SOI. Finally, figure 6 shows the graphs of the 5-month negative running-average  $\overline{PC}'_1(m) = -PC'_1(m-2) - \dots - PC_1(m+2)$  for all months  $m$ , along with the similarly averaged Nino-3 and EPSI indices. In this case, the (unconditional) correlation between the time series Nino-3( $y$ ) and  $\overline{PC}'_1(y+t)$  reaches a maximum of 0.68 when  $t = 2$  months. The same  $t = 2$  months delay applied to  $\overline{PC}'_1(y+t)$  maximizes its correlation with EPSI( $y$ ) at the slightly lower value of 0.65. These results confirm that the global rain anomaly is well correlated with ENSO.

Thus one can conclude that the TRMM record confirms that ENSO is the major driver of the interannual variability of global rainfall. This conclusion should be tempered by two observations.

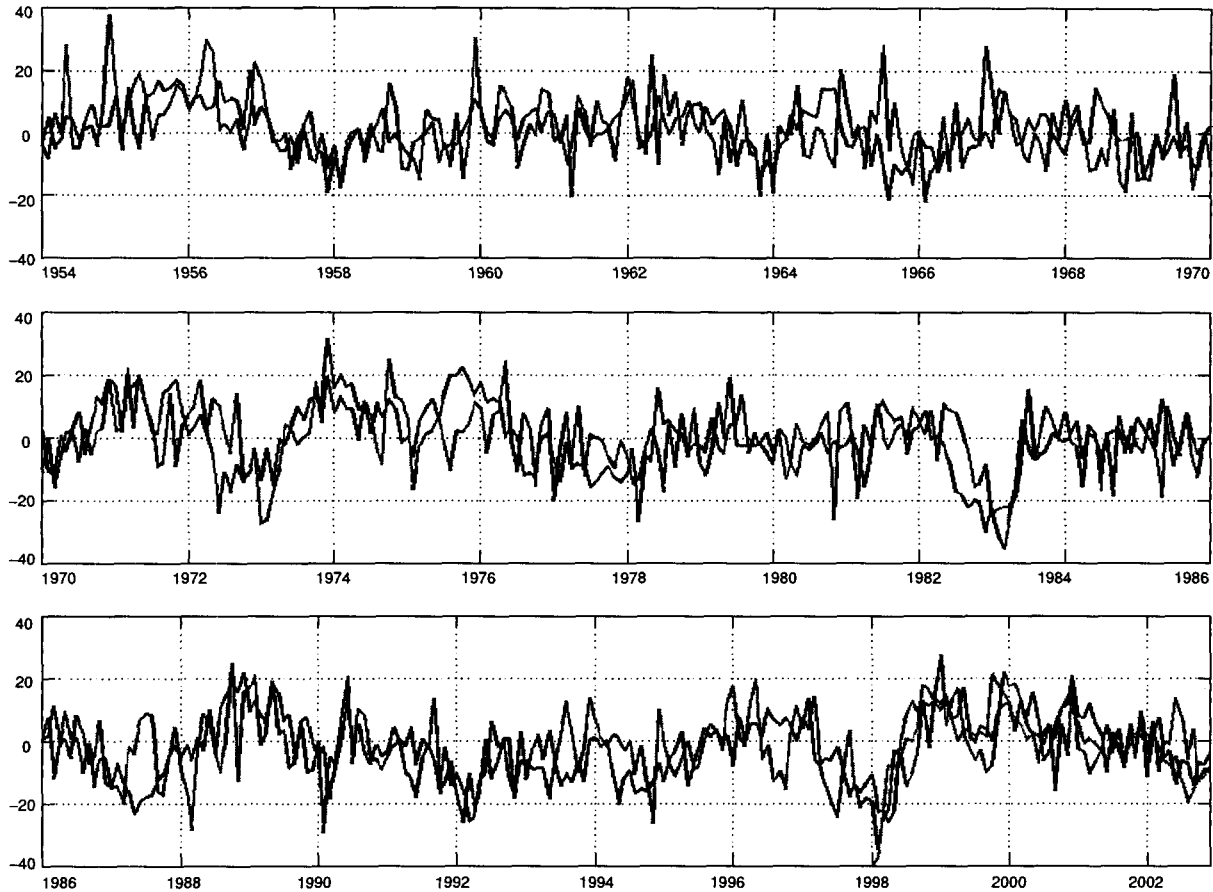


Fig. 5. The time-series of the TRMM-combined anomaly  $PC_1$  (red), its 21-station fit  $PC'_1$  (blue), and the SOI (black).

The first is that the record of TRMM estimates of surface rainfall is geographically restricted to latitudes between  $40^\circ\text{S}$  and  $40^\circ\text{N}$ . Future precipitation remote sensing projects, such as the multinational Global Precipitation Measurement mission's plans for a constellation of satellites, should extend the coverage to a much greater proportion of the globe. The second observation is that our method of extending TRMM's 60-month record to the preceding decades is admittedly approximate and could be greatly improved with the advent of higher-resolution global models. Finally, the principal component analysis does highlight those regions where the installation of denser networks of precise in-situ rainfall-measuring instruments would be most cost-effective in validating the estimates of future remote-sensing missions as well as those of enhanced weather models.

#### References:

Adler, R.F., Negri, A.J., Keehn, P.R., Hakkarinen, I.M., 1993: Estimation of monthly rainfall over Japan and surrounding waters from a combination of low-orbit microwave and geosynchronous IR data. *J. Appl. Met.* **32**, 335-356.

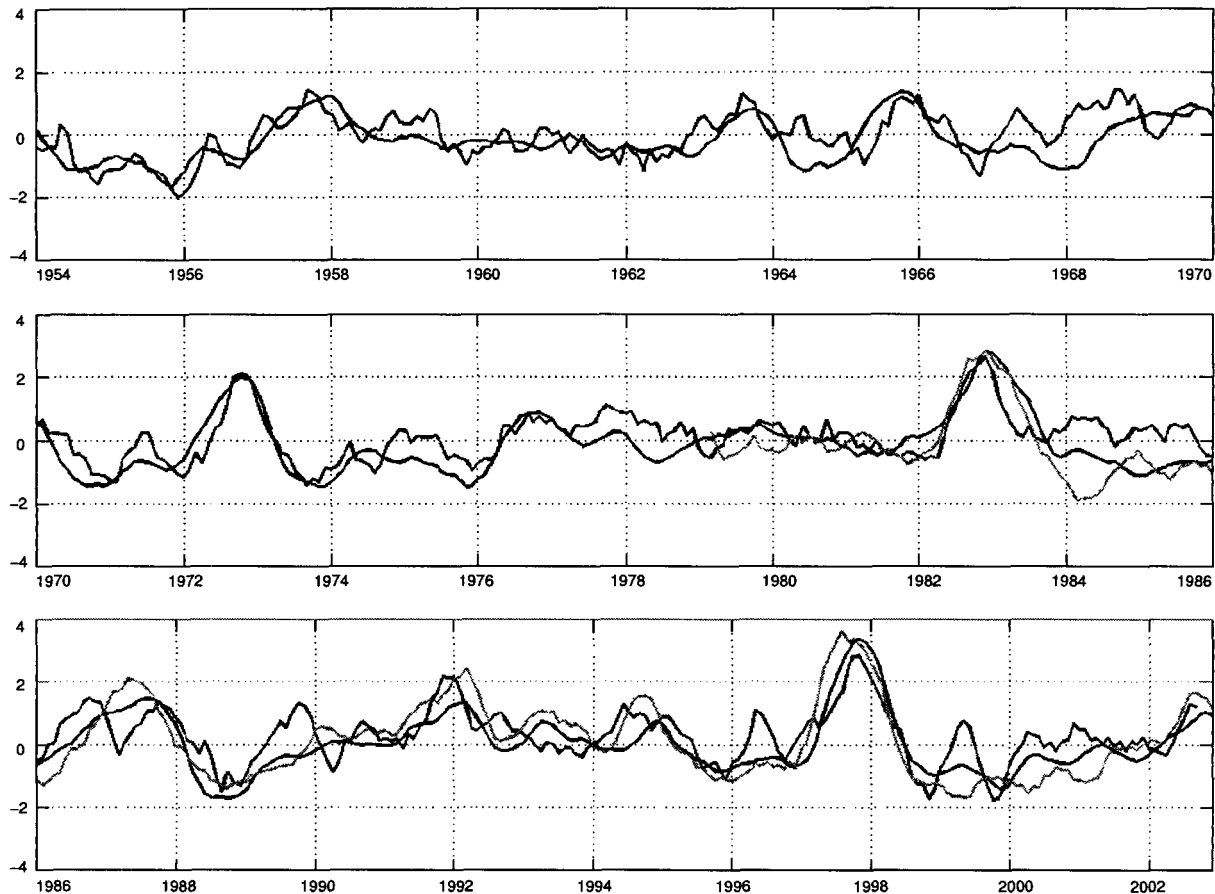


Fig. 6. The TRMM-combined anomaly proxy -  $PC_1'$  (in blue), ESPI (in green) and the Niño-3 index (in black).

Adler, R.F., Huffman, G.J., Bolvin, D.T., Curtis, S., Nelkin, E.J., 2000: Tropical rainfall distributions determined using TRMM combined with other satellite and rain gauge information. *J. Appl. Met.* **39**, 2007-2023.

Arkin, P A., 1979: Relationship between fractional coverage of high cloud and rainfall accumulations during GATE over the B-scale array. *Mon. Wea. Rev.* **107**, 1382-1386.

Arkin, P A., 1982: The relationship between interannual variability in the 200-mb tropical wind field and the Southern Oscillation. *Mon. Wea. Rev.* **110**, 1393-1404.

Bjerknes, J., 1969: Atmospheric teleconnections from equatorial pacific. *Mon. Wea. Rev.* **97**, 163-167.

Curtis, S., Adler, R.F., 2000: ENSO indices based on patterns of satellite-derived precipitation. *J. Clim.* **13**, 2786-2793.

Dai, A., Fung, I.Y., Del Genio, A.D., 1997: Surface observed global land precipitation variations during 1900-88. *J. Clim.* **10**, 2943-2962.

- Dai, A., Wigley, I.M.L., 2000: Global patterns of ENSO-induced precipitation. *Geophys. Res. Lett.* **27**, 1283-1286.
- Haddad, Z.S., Smith, E.A., Kummerow, C.D., Iguchi, T., Farrar, M.R., Durden, S.L., Alves, M., Olson, W.S., 1997: The TRMM day-1 radar/radiometer combined rain-profiling algorithm. *J. Met. Soc. Japan* **75**, 799-809.
- Haddad, Z.S., Rosenfeld, D., 1997: Optimality of Z-R relations. *Q. J. Roy. Met. Soc* **123**, 1283-1293.
- Huffman, G.J., Adler, R.F., Arkin, P., Chang, A., Ferraro, R., Gruber, A., Janowiak, J., McNab, A., Rudolf, B., Schneider, U., 1997: The Global Precipitation Climatology Project (GPCP) combined precipitation dataset. *B. Am. Met. Soc.* **78**, 5-20.
- Peterson, T.C., Vose, R.S., 1997: An overview of the global historical climatology network temperature database. *B. Am. Met. Soc.* **78**, 2837-2849.
- Latif M., Anderson, D., Barnett, T., Cane, M., Kleeman, R., Leetmaa A., O'Brien, J., Rosati, A., Schneider, E., 1998: A review of the predictability and prediction of El Nino. *J. Geophys. Res.* **103**, 14375-14393.
- Ropelewski, C.F., Halpert, M.S., 1987: Global and regional scale precipitation patterns associated with the El-Nino Southern Oscillation. *Mon. Wea. Rev.* **115**, 1606-1626.
- Ropelewski, C.F., Halpert, M.S., 1988: Precipitation patterns associated with the high index phase of the Southern Oscillation. *J. Clim.* **2**, 268-184.
- Simpson, J., Adler, R. F., North, G.R., 1988: A proposed Tropical Rainfall Measuring Mission (TRMM) satellite. *B. Am. Met. Soc.* **69**, 278-295.
- Trenberth, K.E., Stepaniak, D.P., 2001: Indices of El Nino evolution. *J. Clim.* **14**, 1697-1701.
- Troup, A.J., 1965: Southern oscillation. *Q. J. Roy. Met. Soc.* **91**, 490-491.
- Xie, P., Arkin, P.A., 1997: Global precipitation: a 17-year monthly analysis based on gauge observations, satellite estimates, and numerical model outputs. *B. Am. Met. Soc.* **78**, 2539-2558.

**Acknowledgment:**

*This work was performed at the Jet Propulsion Laboratory, California Institute of Technology, under contract with the National Aeronautics and Space Administration.*